Article

Understanding the Electrochemical Reaction Mechanism of the Co/Ni Free Layered Cathode Material P2−Na$_{2/3}$Mn$_{7/12}$Fe$_{1/3}$Ti$_{1/12}$O$_2$ for Sodium-Ion Batteries

Jiali Peng, Angelina Sarapulova, Qiang Fu, Hang Li, Hao Liu, Oleksandr Dolotko, Thomas Bergfeldt, Karin Kleiner, Bixian Ying, Yi Wu, Volodymyr Baran, Edmund Welter, Peter Nagel, Stefan Schuppler, Michael Merz, Michael Knapp, Helmut Ehrenberg, and Sylvio Indris*

Read Online

ACCESS | Metrics & More | Article Recommendations | SI Supporting Information

ABSTRACT: Iron- and manganese-based layered electrodes for sodium-ion batteries have attracted renewed interest due to their low cost and environmental friendliness. However, phase changes at high voltage and the Jahn−Teller effect lead to a short cycle life and poor rate capability. Herein, we describe the optimization of the structure of a Co/Ni free Na$_{2/3}$Mn$_{1/2}$Fe$_{1/2}$O$_2$ cathode via partial substitution of Fe by Mn and Ti and explore the redox activity of P2-type Mn/Fe-based layered cathodes. The obtained P2−Na$_{2/3}$Mn$_{7/12}$Fe$_{1/3}$Ti$_{1/12}$O$_2$ (NMFTO) exhibits a solid solution mechanism during the complete desodiation/resodiation process and delivers an initial discharge capacity of 170 mA h g^{-1} at a 0.1 C rate and a capacity retention of 80% after 50 cycles. The main focus is to understand the electrochemical mechanism of P2−Na$_{2/3}$Mn$_{7/12}$Fe$_{1/3}$Ti$_{1/12}$O$_2$ by exploring the redox processes of transition metal cations and oxygen anions upon cycling. *In situ* synchrotron radiation diffraction reveals a single-phase reaction of NMFTO during cycling, which is beneficial to improving cycle stability. *In situ* X-ray absorption spectroscopy (XAS), *in situ* ^{57}Fe Mössbauer spectroscopy, and *ex situ* ^{23}Na nuclear magnetic resonance spectroscopy are used to elucidate the changes in the crystallographic/electronic structure during desodiation/resodiation. *Ex situ* soft XAS reveals the participation of oxygen anions in the electrochemical reactions.
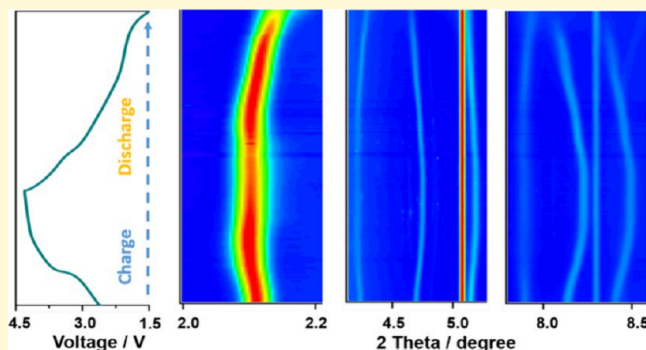
1. INTRODUCTION

Sodium-ion batteries (SIBs) are a low-cost alternative to lithium-ion batteries (LIBs) in large-scale electric energy storage applications due to the natural-abundant sodium resources and similar working principles to LIBs during cycling.[1−3] Until now, many different cathodes for SIBs have been studied, including layered transition metal (TM) oxides (Na$_x$TMO$_2$, $x \leq 1$), Prussian blue-type compounds, and polyanionic and organic compounds.[4] Among them, Na$_x$TMO$_2$ has been extensively reported due to its layered structure, facile synthesis, promising electrochemical properties, and feasibility for commercial production.[5−8] The classification of layered oxides into O3, P2, and P3 types is based on the coordination environment of Na cations, which can be found in either octahedral or prismatic sites, and the stacking order of different oxygen layers such as ABCABC, ABBA, and ABBCCA.[9] At low potentials (<2.0 V vs Na/Na$^+$), there is a phase transition P2−P′2 connected with the manganese redox activity and a significant Jahn−Teller distortion.[10] Compared with the O3-type structure, P2-type Na$_x$TMO$_2$ provides better structural stability.[11] The lower
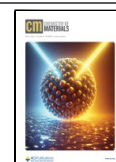
diffusion barriers in P2-type Na$_x$TMO$_2$ are associated with prismatic sites of Na ions.[12] P2-type materials undergo phase transitions upon cycling, leading to short cycle life and poor rate capability.[13] A first approach to alleviate the limits of P2-type cathodes is limiting the upper cutoff voltage to 4.1 V to avoid the P2−O2 transition.[14] The second approach is chemical modification, which can suppress structural transitions at higher voltages. The initial report about P2-type Na$_{2/3}$Mn$_{1/2}$Fe$_{1/2}$O$_2$ (NMFO) is from Komaba's group, which demonstrated the activity of Fe^{3+}/Fe^{4+} redox couple during cycling. However, structural transitions result in poor capacity retention.[15−17] To address this challenge, replacing TM atoms in the TMO$_2$ slabs such as Ni-substituted and Mn/Ni cosubstituted P2−Na$_x$[Fe$_{0.5−2y}$Ni$_y$Mn$_{0.5+y}$]O$_2$ have been dem-

onstrated as an effective strategy to suppress these structural changes over a wider compositional range. As one example from the literature, Zn-doping prevents the phase transition of $Na_{0.60}Fe_{0.5}Mn_{0.5}O_2$ cathodes from P2 to OP4 (i.e., alternating stacking of octahedral and prismatic Na sites along the c axis) during cycling.[18] $P'2\text{-}Na_{0.67}[(Mn_{0.78}Fe_{0.22})_{0.9}Ti_{0.1}]O_2$ was reported by Myung's group in 2019 and Ti was used to substitute both Mn and Fe to minimize the phase transition of $P'2\text{-}Na_{0.67}[Fe_xMn_{1-x}]O_2$ during cycling.[2] The authors claimed that the introduction of Ti^{4+} in the $P'2\text{-}Na_{0.67}[(Mn_{0.78}Fe_{0.22})_{0.9}Ti_{0.1}]O_2$ successfully suppresses the phase transition from $P'2$ to OP4, as evidenced by *in situ* synchrotron X-ray diffraction (SXRD), which revealed the occurrence of a single phase reaction during cycling. The suppression of the $P'2$ to OP4 phase transition may have contributed to the delivery of high capacity even at high rates and excellent capacity retention with prolonged cycling.[2] Compared with NMFO, P2-type $Na_{2/3}Mn_{2/3}Fe_{1/3}O_2$ merely shows stacking fault distortions instead of a phase transition from P2-Z during cycling, where Z is a low-crystallinity phase which can be characterized as an evolving intergrowth that includes varying ratios of P2, O2, and OP4 structures, progressing from P2 through OP4 to O2 during the charging process (Na extraction).[19−21] This can improve the capacity retention.[22] Nevertheless, the remaining $P'2$ phase with space group *Cmcm* observed in the low potential range leads to anisotropic strain in the layered structure and deteriorates the electrochemical performance.[23] One way to avoid the Jahn−Teller distortion is to increase the lower cutoff voltage to a value higher than 2.0 V with compromised specific capacity.[24] Moreover, the insertion of electrochemically inactive elements (Al,[25] Mg[26]) into the layered oxide structure is an effective approach to mitigate Jahn−Teller distortion and enhance cycling performance. Yang et al. introduced Ti doping into $Na_{2/3}Fe_{1/3}Mn_{2/3}O_2$ to suppress the Jahn−Teller distortion and improve both cycling and rate performance and $P2-Na_{2/3}Fe_{1/3}Mn_{0.57}Ti_{0.1}O_2$ undergoes a single-phase reaction and maintains the single P2 phase during cylcling, as evidenced by *in situ* synchrotron X-ray diffraction. In addition, XPS analysis was applied to explore the influence of Ti doping on the valence composition, which can only provide information from the surface of the electrode materials.[24]

Meanwhile, anionic redox activity, which has been frequently reported for LIBs, is also involved in the electrochemical process in a few cathode materials for SIBs. For example, Ma et al. provided evidence of the participation of oxygen anions in the charge compensation process of the high energy P2-type $Na_{0.78}Ni_{0.23}Mn_{0.69}O_2$ cathode material by electron energy loss spectroscopy (EELS) and soft X-ray absorption spectroscopy (sXAS).[27] The first peak in the EELS spectra at an energy loss of 532 eV obtained at the surface of cycled particles almost vanishes. The decrease in intensity of the oxygen prepeak at the surface of cycled particles can be attributed to the electronic transition from the 1s core state to the O 2p-TM 3d hybridized states, indicating fewer holes in the 2p-3d hybridized orbitals and suggesting that surface transition metals are in a lower valence state. The observed sXAS spectra for cycled particles indicate that lattice oxygen redox processes take place upon charge. Maitra et al. claimed that during the charging period when x has dropped below ∼0.53, the additional capacity obtained for $Na_xMg_{0.28}Mn_{0.72}O_2$ (beyond what can be expected from just the transition metals)

must correspond to the removal of electrons from oxygen and the creation of electron−hole states on the O.[28]

Herein, we present a structure optimization of the P2-type layered NMFO positive electrode material via a partial substitution of Fe by Mn and Ti to explore the electrochemical mechanism of redox activity of P2-type Mn/Fe based layered cathodes. The NMFO cathode exhibits subsequent phase transitions P2 → P2/Z → Z → Z/P2 → P2 → P'2 during cycling.[29] However, in the modified NMFTO structure, the additional Mn^{4+} and Ti^{4+} cations in the TM layers can suppress the P2-Z phase transition and decrease the extent of distortions in the structure. The similar ionic radii and the same valence of Mn^{4+} and Ti^{4+} ensure a homogeneous incorporation of Ti^{4+} into the TM layers. As a result, the Mn^{4+}/Ti^{4+} cosubstituted material (NMFTO) exhibits a single P2 phase during the whole charging/discharging process as revealed by *in situ* synchrotron radiation diffraction (SRD). *In situ* ^{57}Fe Mössbauer spectroscopy and *in situ* X-ray absorption spectroscopy (XAS) are used to characterize the reversible oxidation of Fe^{3+} to Fe^{4+}. The oxidation of Mn is also observed by *in situ* XAS. Moreover, *ex situ* ^{23}Na nuclear magnetic resonance (NMR) spectroscopy and *ex situ* soft X-ray absorption spectroscopy (sXAS) are performed to investigate the changes in the Na environments and the participation of oxygen anions during electrochemical cycling, respectively.

2. EXPERIMENTAL SECTION

2.1. Materials Synthesis. NMFO and NMFTO phases were synthesized by a solid-state method from stoichiometric amounts of Na_2O_2 (Alfa Aesar, 99%), Mn_2O_3 (Sigma-Aldrich, 99%), Fe_2O_3 (Sigma-Aldrich, 99%), and TiO_2 (Sigma-Aldrich, 99.8%) with molar ratios of 2/3:1/2:1/2 and 2/3:7/12:1/3:1/12, respectively. For each composition, the mixture was pelletized and heated at 850 °C for 12 h in air. Due to the sensitivity against ambient atmosphere, samples then were quenched to room temperature and stored in an Ar-filled glovebox until use. The morphology of the as-synthesized materials was observed by using a scanning electron microscope (SEM, Zeiss Merlin). The powder X-ray diffraction (XRD) patterns were collected using a STOE STADI P diffractometer with Mo $K\alpha1$ radiation (λ = 0.709320 Å) in a scanning range of 4°−50°. The XRD data of NMFO and NMFTO were analyzed using Rietveld refinement. The FullProf software package was utilized.[30] Berar & Lelann corrected estimated standard deviations are given for the refined parameters.[31]

2.2. Materials Characterization. High-resolution *in situ* SRD experiments on NMFO and NMFTO were performed with a photon energy of 60 keV (λ = 0.2072 Å) at beamline P02.1, storage ring PETRA III at Deutsches Elektronensynchrotron (DESY) in Hamburg, Germany.[32] The diffraction patterns were acquired using a VAREX XRD 4343CT (150 × 150 μm^2 pixel size, 2880 × 2880 pixel area) 2D position-sensitive detector. The exposure time for each pattern was 60 s. CR2032 coin cells with glass windows (diameter of 6 mm) were used. Data calibration (LaB$_6$, NIST-660c) and integration were done using the DawnSci software.[33]

^{23}Na magic-angle spinning nuclear magnetic resonance (MAS NMR) experiments were performed at a Bruker Avance neo 200 MHz spectrometer at a field of 4.7 T using a 1.3 mm MAS probe at a spinning speed of 60 kHz. The recycle delay was set to 1 s, and the Larmor frequency was 52.9 MHz. ^{23}Na MAS NMR spectra were acquired by using a rotor-synchronized Hahn-echo pulse sequence (90°−τ−180°−τ−acquisition) with a 90° pulse length of 0.95 μs. Spectral intensities were normalized with respect to sample mass and number of scans.

In situ XAS analysis on NMFO and NMFTO positive electrodes were performed during charging/discharging using a cell design similar to that used for the *in situ* XRD studies. XAS was performed at beamline P65 at PETRA-III, Germany. Electrochemical cycling was
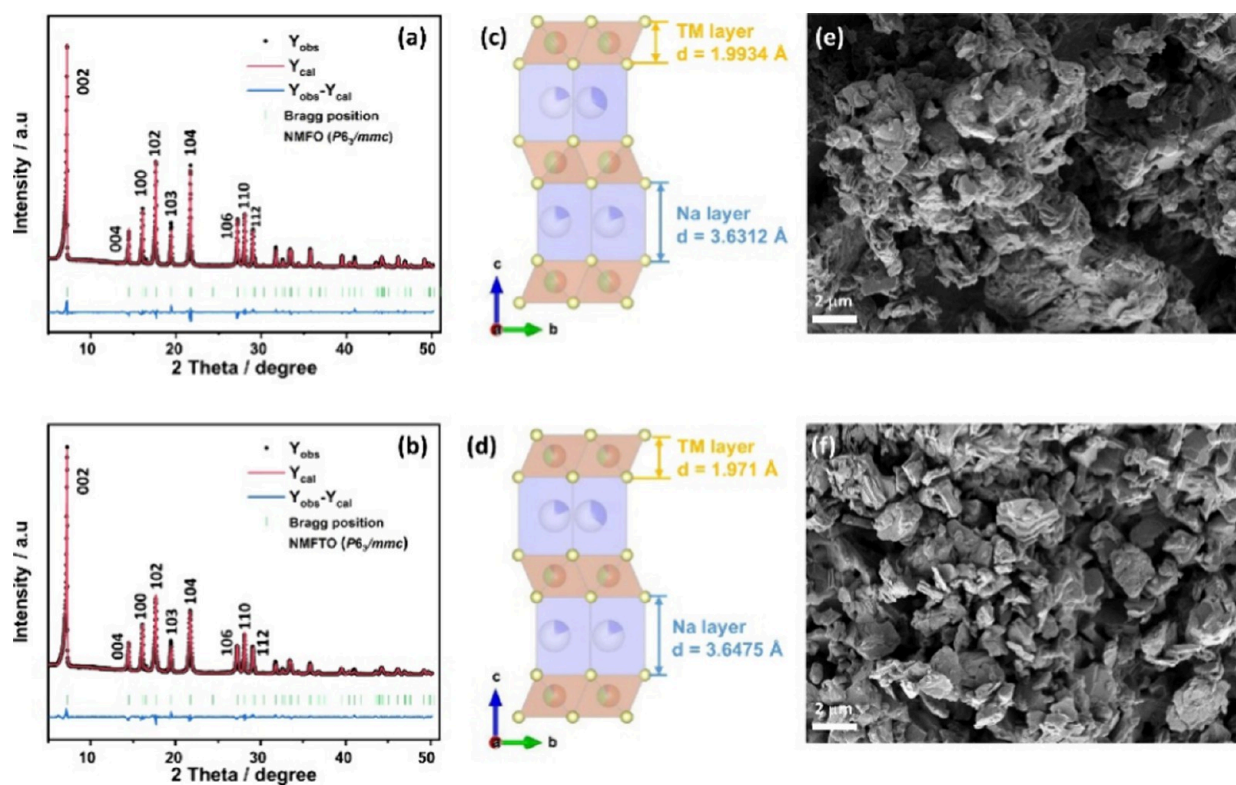
Figure 1. Rietveld refinement based on XRD diffraction (λ = 0.71 Å) of cathode materials (a) NMFO and (b) NMFTO. Crystal structures of (c) NMFO and (d) NMFTO. SEM images of pristine (e) NMFO and (f) NMFTO.

conducted in 2032-type coin cells with a 6 mm Kapton window in the voltage range of 1.5−4.3 V. XAS spectra at the Fe K-edge and Mn K-edge were acquired with a beam size of 0.3 × 1.5 mm². All XAS spectra were analyzed and processed utilizing the ATHENA software package.[34]

^{57}Fe Mössbaur spectra were collected at room temperature with a constant-acceleration spectrometer in transmission mode and a ^{57}Fe (Rh) source. All isomer shifts were given relative to those of α-Fe metal. Synthesis of the cathode materials was done with Fe$_2$O$_3$ enriched in ^{57}Fe (95%). The NMFO and NMFTO powder together with the conductive carbon (C65) and poly(vinylidene difluoride) (PVDF) binder in a weight ratio of 8:1:1 was mixed in 1-methyl-2-pyrrolidone (NMP) and cast onto Al foil. After drying at 80 °C, electrode tapes were cut into discs of 19 mm diameter, pressed with a hydraulic press at 6 tons, and dried at 120 °C under vacuum overnight. Electrochemical cycling was conducted in special cells with a 14 mm Kapton window in the voltage range of 1.5−4.3 V.

Soft X-ray measurements were carried out at the beamline WERA at the KIT light source in Karlsruhe, Germany. The measurements were conducted on electrodes that were charged or discharged to different voltages. Data were acquired in fluorescence yield (FY) and inverse partial fluorescence yield (IPFY) mode using a low-energy 4-channel silicon drift detector.

The crystal structure and elemental distribution of the samples were measured by high-resolution transmission electron microscopy (HRTEM) and high-angle annular dark-field scanning transmission electron microscopy (HAADF-STEM)-energy dispersive X-ray spectroscopy (EDS) mapping measurements at 300 kV acceleration voltage using a Thermo-Fisher Themis-Z equipped with double aberration correctors (TEM and STEM).

2.3. Electrochemical Characterization. To prepare electrodes, the obtained powder (NMFO and NMFTO) together with conductive carbon (C65) and poly(vinylidene difluoride) (PVDF) binder were mixed in a weight ratio of 8:1:1 in 1-methyl-2-pyrrolidone (NMP) and cast onto Al foil. After drying at 80 °C, electrode tapes were cut into discs of 12 mm diameter, pressed with a hydraulic press

at 6 tons, and dried at 120 °C under vacuum overnight. The average mass loading was approximately 5 mg for both materials. Metallic sodium foil served as a counter electrode, and the electrodes were measured in 2032-type two-electrode coin cells. One molar NaClO$_4$ in a 1:1 (v:v) ratio of ethylene carbonate/dimethyl carbonate (EC/DMC) with 5 wt % fluoroethylene carbonate (FEC) was used as electrolyte. The cells were galvanostatically charged and discharged with a Biologic potentiostat at different C rates between 1.5 and 4.3 V at 25 °C.

For the GITT measurement, short current pulses were applied to the cell with a resting time of 5 h inserted after each pulse. The diffusion coefficient could be calculated based on the following equation:[35]

$$D_s = \frac{4}{\pi}\left(\frac{IV_m}{FS}\right)^2\left(\frac{dU°/dy}{dV/d\sqrt{t}}\right)^2, \; t \ll R^2/D_s$$

where I is the current value for the short pulse, F is Faraday's constant, V_m is the molar volume of the NMFO or NMFTO active material, S is the composite electrode active area, $U°$ is the open-circuit potential at the end of each rest period, y is the state of charge (SoC), V and t are the voltage and time during pulse periods, and R is the diffusion length. Instead of giving the absolute diffusion coefficients, $D_s S^2/V_m^2$ was calculated since the molar volume (V_m) and active surface area (S) are difficult to obtain. Two additional GITT experiments were conducted to increase the reliability of the conclusions.

3. RESULTS AND DISCUSSION

Both P2-type layered compounds NMFO and NMFTO were synthesized as single-phase material. The atomic compositions of the samples were measured by inductively coupled plasma-optical emission spectroscopy (ICP-OES), and the results are listed in Table S1. The results for the TM ratios were almost identical with the targeted values as expressed by the chemical formulas Na$_{2/3}$Mn$_{1/2}$Fe$_{1/2}$O$_2$ (NMFO) and
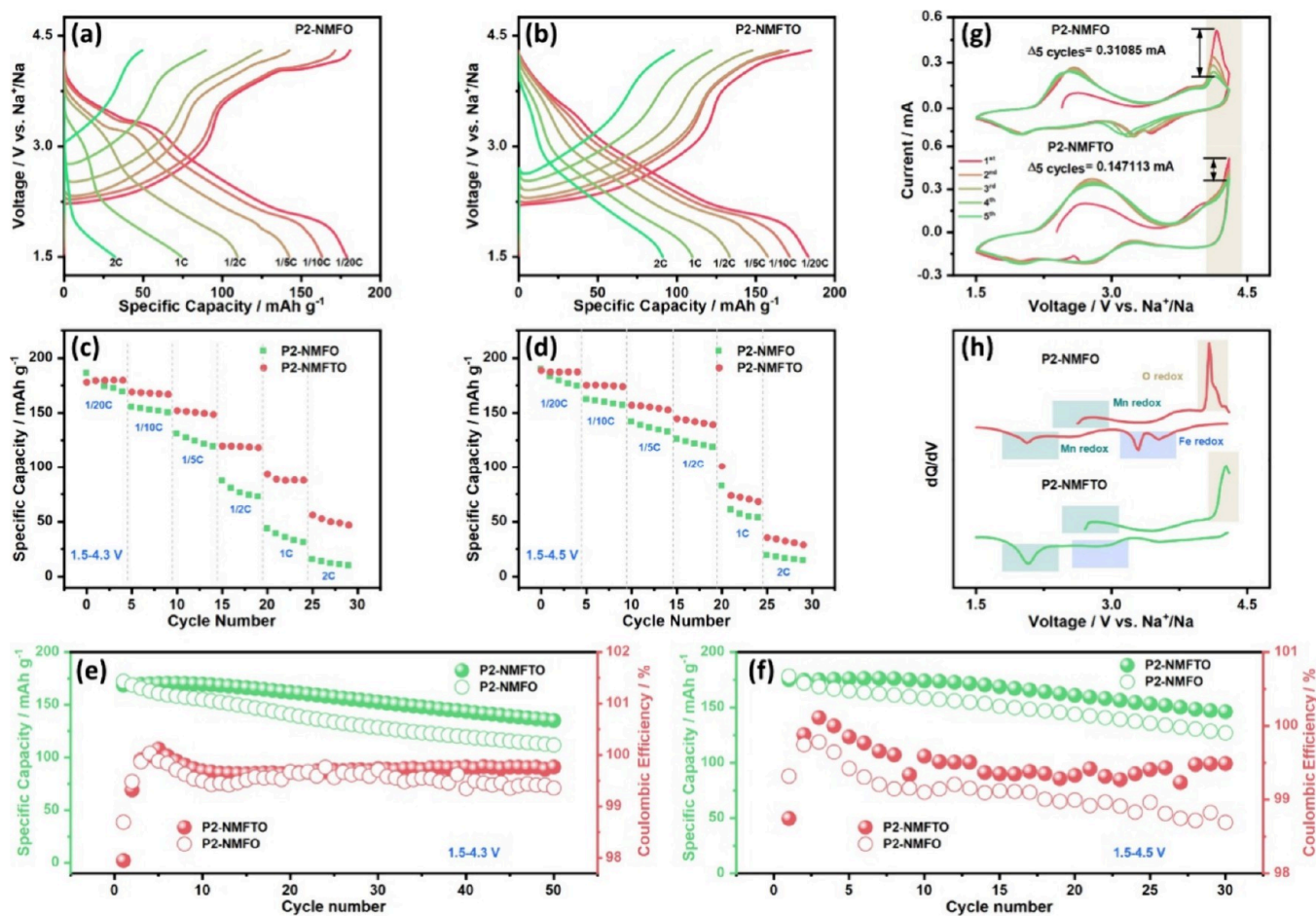
Figure 2. Charge/discharge curves at rates between 0.05 and 2 C of (a) NMFO and (b) NMFTO; rate capability of NMFO and NMFTO at rates between 0.05 and 2 C in voltage windows of (c) 1.5−4.3 V and (d) 1.5−4.5 V; (e) first five CV curves of NMFO and NMFTO at 0.1 mV/s in the voltage range of 1.5−4.3 V; (f) dQ/dV curves of NMFO and NMFTO at 0.1 C; cycling performance of NMFO and NMFTO at 0.1 C in voltage windows of (g) 1.5−4.3 V and (h) 1.5−4.5 V.

$Na_{2/3}Mn_{7/12}Fe_{1/3}Ti_{1/12}O_2$ (NMFTO). The Na/TM ratio for both materials is around 0.66, which is again very close to the targeted value of 0.67. X-ray diffraction (XRD) patterns (Figure 1a,b) show that all reflections of these two materials can be ascribed to a hexagonal lattice with space group $P6_3/mmc$, which is isostructural with P2-type Na_xCoO_2.[36] The unit cell parameters of NMFO ($a = b = 2.92410(7)$ Å, $c = 11.24914(52)$ Å) turn out to be slightly larger than those of the substituted NMFTO ($a = b = 2.91911(11)$ Å, $c = 11.23690(102)$ Å). The obtained crystallographic characteristics for both materials are given in Table S2. The crystal structure illustration of both materials is shown in Figure 1c (NMFO) and Figure 1d (NMFTO). The increased sodium interlayer spacing of the substituted material can promote Na^+ intercalation/deintercalation. The radii of Ti^{4+} (0.605 Å) and Mn^{4+} (0.53 Å) are smaller than that of Fe^{3+} (0.645 Å),[37] which leads to the reduced slab thickness of the TM layer of the substituted material. The primary particle size of both materials is approximately 500 nm, as shown in Figure 1e,f, and these primary particles are agglomerated, forming several micrometer-sized secondary particles. SEM-EDX mappings of both materials are shown in Figures S1 and S2. The EDX mappings of NMFO and NMFTO demonstrate that the elements are homogeneously distributed over the particles. A high-resolution transmission electron microscopy (HRTEM) image (Figure S3b) of NMFO displays two sets of lattice

fringes with d-spacings of 0.247 and 0.253 nm, which can be indexed to the (111) and (010) planes of the $P6_3/mmc$ symmetry. The HRTEM image of NMFTO shown in Figure S4b displays two sets of lattice fringes with d-spacings of 0.246 and 0.252 nm, which are very similar to the values of the unsubstituted material. This is in good agreement with the XRD results where the differences in the a and c lattice parameters between both samples was 0.2% and 0.1%, respectively. The corresponding fast Fourier transform (FFT) patterns (Figures S3c and S4c) exhibit an array of dots with hexagonal symmetry. The high-angle annular dark-field scanning transmission electron microscopy (HAADF-STEM) together with energy dispersive X-ray spectroscopy (EDX) demonstrates that the elements are homogeneously distributed over the particles for both NMFO (Figure S3a,d−g) and NMFTO (Figure S4a,d−h).

Figure 2 displays the results of electrochemical cycling for both cathodes against Na metal counter electrodes. The rate capabilities at rates between 0.05 and 2 C are shown for P2-NMFO and P2-NMFTO in Figure 2a and Figure 2b, respectively. In comparison to the slower cycling at 0.05 C (in the voltage range 1.5−4.3 V), NMFO delivers approximately 18.7% of specific capacity for fast cycling at 2 C, while it is 42% for P2-NMFTO. This confirms that the rate capability of the substituted material is much better than that of the unsubstitutes material. The charge/discharge curves at differ-

ent rates show that the capacity is reduced and the polarization is increased with increasing current density. However, the effects for the substituted NMFTO are far less pronounced than that for unsubstituted NMFO. As shown in Figure S5a,d, compared to those for NMFO, the curves of NMFTO show much smaller polarization during cycling, which confirms the high cycling stability of the substituted material.

Moreover, the rate performance of both cathodes at different rates is compared in Figure 2c (voltage window: 1.5−4.3 V) and Figure 2d (voltage window: 1.5−4.5 V). The capacities of NMFTO are 180 mAh g^{-1}, 169 mAh g^{-1}, 152 mAh g^{-1}, 120 mAh g^{-1}, 93.3 mAh g^{-1}, and 56 mAh g^{-1} at 0.05, 0.1, 0.2, 0.5, 1, and 2 C, respectively, in the voltage range of 1.5−4.3 V. However, for NMFO, only 15.3 mA h^{-1} is obtained at 2 C. Figure 2d shows the capacities of both materials at different rates in the voltage range 1.5−4.5 V, which reveals that the substituted NMFTO has higher capacities and better rate performance than the unsubstituted material, even in this larger voltage window. The cycling performance of NMFO and NMFTO in the voltage range of 1.5−4.3 V at 0.1 C is compared in Figure 2e. NMFTO has a significantly improved cycling stability with an initial discharge capacity of 170 mA h g^{-1} at 0.1 C and a capacity retention of 80% after 50 cycles, while the capacity retention of NMFO is just 64.9%. The cycling performance is also tested in the voltage range 1.5−4.5 V to compare the stability of both materials at higher working voltages, as shown in Figure 2f. The capacity retention of NMFTO is 83.4% after 30 cycles, and it is only 71.1% for NMFO. The electrochemical performance comparison of reported iron- and manganese-based cathodes and materials described in this paper are summarized in Table S3, which shows that Ti substituted P2-NMFTO has better cycling stability than most iron- and manganese-based cathodes. The cycling performance of NMFO and NMFTO at 1 C in the voltage window 1.5−4.5 V is displayed in Figure S6. The results reveal that substituted NMFTO has a better cycling stability even in the higher potential range and at a higher scan rate.

Figure 2g shows the first five cyclic voltammogram (CV) curves of NMFO and NMFTO at a scan rate of 0.1 mV s^{-1}. For NMFO, the reduction in peak intensity involving O oxidation at about 4.25 V after five cycles is larger than for NMFTO.[38,39] The loss of O in NMFO at high voltages results in a rapid decrease in the level of O-redox activity in the following cycles. The oxidation and reduction peaks of NMFTO show very small polarization after cycling, which reveals the improved stability, lower polarization, and more reversible cationic redox of the substituted materials.[39] The first five CV cycles of NMFO (Figure S7a) and NMFTO (Figure S7b) at 0.1 mV s^{-1} in the voltage window of 1.5−4.5 V show that the oxidation and reduction peaks of NMFTO after cycling in a larger voltage window show polarization that is even smaller than that for the unsubstituted material, especially for the Fe reduction peaks observed at 2.8 V. Figure 2h presents the dQ/dV result of NMFO and NMFTO in the potential range of 1.5−4.3 V. The Mn oxidation and reduction peaks for NMFO are observed at around 2.6 and 2.0 V. The Mn oxidation peak for NMFTO is located at around 2.75 V, which reveals that the oxidation of Mn occurs a little bit later than for NMFO. The peak belonging to Fe reduction occurs around 3.25 V. However, the Fe reduction peak of NMFO is more pronounced than that of NMFTO. Oxidation of oxide ions occurs at the end of the charge and the reaction in NMFO

occurs earlier than in NMFTO. Figure S8 shows the dQ/dV curves of NMFO and NMFTO at a scan rate of 0.1 mV s^{-1} in the voltage ranges of 1.5−4.3 and 1.5−4.5 V. For NMFO (Figure S8a), when the cathode is charged to higher voltages, the Fe reduction peak shows a drastic change, while the corresponding peaks of NMFTO (Figure S8b) are very stable, which indicates the better structural stability of the substituted material even in the wider potential window.

In order to explain the better performance of substituted NMFTO, in situ and ex situ measurements were performed to explore the overall reaction mechanism. The structural evolution of NMFO and NMFTO during Na$^+$ deintercalation/reintercalation was investigated by in situ SRD measurements at a 0.1 C rate in the voltage range 1.5−4.3 V, as shown in Figure 3. From the open circuit voltage (OCV) to 4.1 V, the
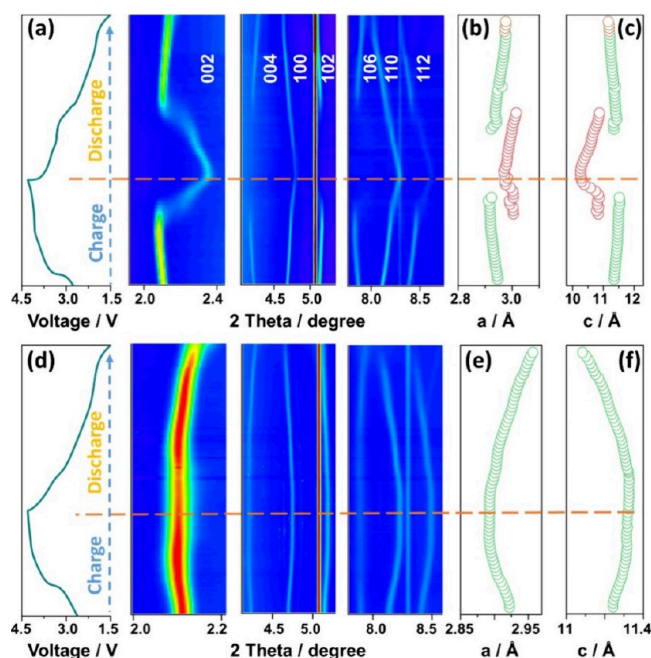

Figure 3. Contour maps (a) of in situ synchrotron diffraction data collected during the first charge/discharge process and the corresponding voltage profiles on the left side and the changes of the lattice parameters on the right side (b, c) for NMFO at 0.1 C rate and over the range of 1.5−4.3 V and the corresponding data for NMFTO (d−f). The error bars of the lattice constants a and c are much smaller than the size of the markers used in panels (b, c, e, f).

002, 004, and 106 reflections of NFMO shifted to lower angles, reflecting a gradual expansion of the interlayer spacing (Figure 3c). At the same time, the 100, 102, 110, and 112 reflections are shifted toward larger angles, revealing a contraction of the distances within the layer (Figure 3b). When the NMFO cathode is charged to voltages above 4.1 V, new reflections appear indicating the phase transition in this material, due to the gliding of [Fe$_{1/2}$Mn$_{1/2}$]O$_2$ slabs.[29] This phase transition is the transition from the P2 to the Z structure, as reported previously for P2−Na$_x$[Fe$_{1/2}$Mn$_{1/2}$]O$_2$.[29] Upon further charging, the reflections of P2 disappear due to the formation of the Z phase. This phase transition is reversibly achieved by gliding of the TM slabs, which is attributed to the thermodynamic instability of unoccupied prismatic sites. Rietveld refinements against the in situ SRD patterns show that the lattice parameter a (Figure 3b) initially decreases, while the lattice parameter c

(Figure 3c) increases which is in good agreement with previous results on P2-NMFO.[15] According to the contour maps and corresponding cell parameters, no phase change occurs for NMFO during the initial desodation process up to ~4.1 V. In the following discharging to 3.1 V, the positive electrode changes back from the Z to the P2 phase. During further discharging to 1.9 V, a new orthorhombic phase P′2 starts to appear because of the reduction of Mn^{4+} to Jahn–Teller distorted Mn^{3+}. The evolutions of the XRD diffraction patterns of NMFO during charging/discharging and the Rietveld refinement of P′2-NMFO are shown in Figure S9a,b.

In stark contrast, the contour maps of NMFTO (Figure 3d) demonstrate that all reflections show only shifts, and no new reflections appear during the whole charging/discharging process, implying a solid-solution behavior upon Na^+ deintercalation/reintercalation. During the charging process of NMFTO, the 002, 004, and 106 reflections are shifted to lower angles, and they are shifted back to higher angles during the discharging process, again revealing the changes of the interlayer spacings (Figure 3f). Meanwhile, the 100, 102, 110, and 112 reflections are shifted toward higher angles showing a gradual contraction of the in-plane distances during the charging process, and they are shifted back to lower angles during the discharging process (Figure 3e). As reported in earlier work,[24] no P2 → Z phase change occurs for $Na_{2/3}Mn_{2/3}Fe_{1/3}O_2$ at highly charged states, i.e., Mn substitution can suppress sliding of the TMO_2 slabs. At the same time, Ti substitution in NMFO can suppress the formation of the P′2 phase in deeply discharged states, thus improving the capacity retention during cycling.[24]

The XRD diffraction patterns of NMFO and NMFTO are shown in Figure S10a,b for the pristine state, after one full cycle, and after two full cycles in two different voltage ranges at 1.5−4.3 and 1.5−4.5 V, respectively. For the smaller voltage range 1.5−4.3 V, the XRD patterns obtained for the pristine electrode and after one or two cycles do not show significant changes for both materials. However, when the cathodes are charged to 4.5 V, the patterns for NMFTO in the discharged state after one and two cycles show higher stability, i.e., much smaller changes compared to the pristine state, than the unsubstituted NMFO material. The latter one shows a strong line broadening but also appearance/disappearance of reflections. These results reveal that Mn^{4+}/Ti^{4+} substitution can increase the stability of such materials toward higher voltages.

To investigate the local structural changes in more detail, *ex situ* solid state ^{23}Na MAS NMR measurements were performed on as-synthesized NMFO and NMFTO cathodes and on electrodes extracted from cells after charging/discharging to different voltages during the first cycle (Figure 4a−d). The spectrum of pristine NMFO (Figure 4b) shows a major resonance at about 1850 ppm. A much narrower signal close to 0 ppm indicates the presence of small amounts of diamagnetic impurities, such as $NaOH/Na_2CO_3$. These are probably residues from the electrolyte or its decomposition products[26,40−42] For the spectrum of pristine NMFTO (Figure 4d), the major resonance is located at around 1500 ppm. The comparison of the spectra of pristine NMFO and pristine NMFTO is shown in Figure S11. The decrease of the ^{23}Na NMR shift in NMFTO compared to NMFO is caused by the substitution of diamagnetic Ti^{4+} for highly paramagnetic Fe^{3+} centers with large magnetic moments in the environment around Na.[43,44] According to the elemental composition, the
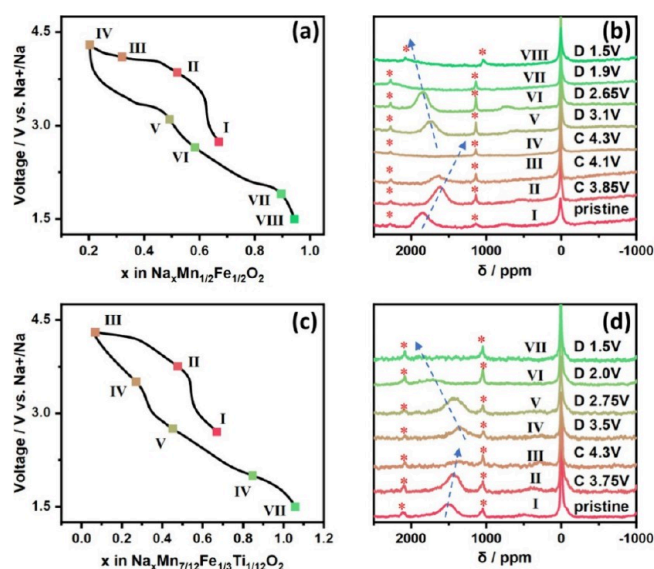

Figure 4. Cell voltage as a function of the state of charge and discharge for the first galvanostatic cycle of (a) NMFO and (c) NMFTO cells; marked points indicate voltages where cells were disassembled for solid-state NMR measurements. ^{23}Na MAS NMR spectra of the (b) NMFO and (d) NMFTO cathode samples. Spinning sidebands are denoted with "*".

average oxidation state of Mn in pristine NMFO is +3.66 and +3.43 in NMFTO (as shown below with Mössbauer spectroscopy, the oxidation state of Fe is +3 in the pristine state for both materials). As a general trend, during the charging process, the major resonance in the ^{23}Na NMR spectra moves to the right (lower ppm values) and back to the left during discharging. The right shift during charging is caused by the oxidation of high-spin Fe^{3+} (electronic configuration $3d^5$) to Fe^{4+} ($3d^4$) and oxidation of Mn^{3+} ($3d^4$) to Mn^{4+} ($3d^3$) resulting in less unpaired electronic spins. During the whole charging process, a clear decrease in the intensity of this major resonance is observed since more and more Na is removed from the material and finally, at 4.3 V, the signal completely disappears, revealing that most of the Na is removed from the structure. During discharging, the ^{23}Na resonance shifts back to higher ppm values due to the reduction of Fe^{4+} to Fe^{3+} and Mn^{4+} to Mn^{3+}. When the NMFO is completely discharged to 1.9 V, the ^{23}Na signal becomes very broad and almost invisible. As shown above via *in situ* SRD, the P′2 phase starts to appear at around 1.9 V, which means that local distortions around Mn occur that can cause this extreme broadening and which can also reduce the mobility of Na^+. ^{23}Na has a quadrupolar nucleus (spin $I = 3/2$) with quite large quadrupolar moment ($Q = 104$ mb)[45] and thus it is very sensitive to local structural distortions which cause the line broadening. The resulting decrease in Na mobility can further broaden the spectra. The evolution of the ^{23}Na NMR spectra during this complete cycle clearly shows that after the full discharge the cathode material is reduced to a state beyond the pristine state, as also expected from the voltage profile, i.e., after the reversible changes observed in the spectra, an additional reduction of the material is observed associated with a sodiation above the initial Na content of 0.67.

For NMFTO (Figure 4d), during the charging period, the main resonance again is shifted to lower values due to the oxidation of Fe and Mn. Even in the fully charged state, some
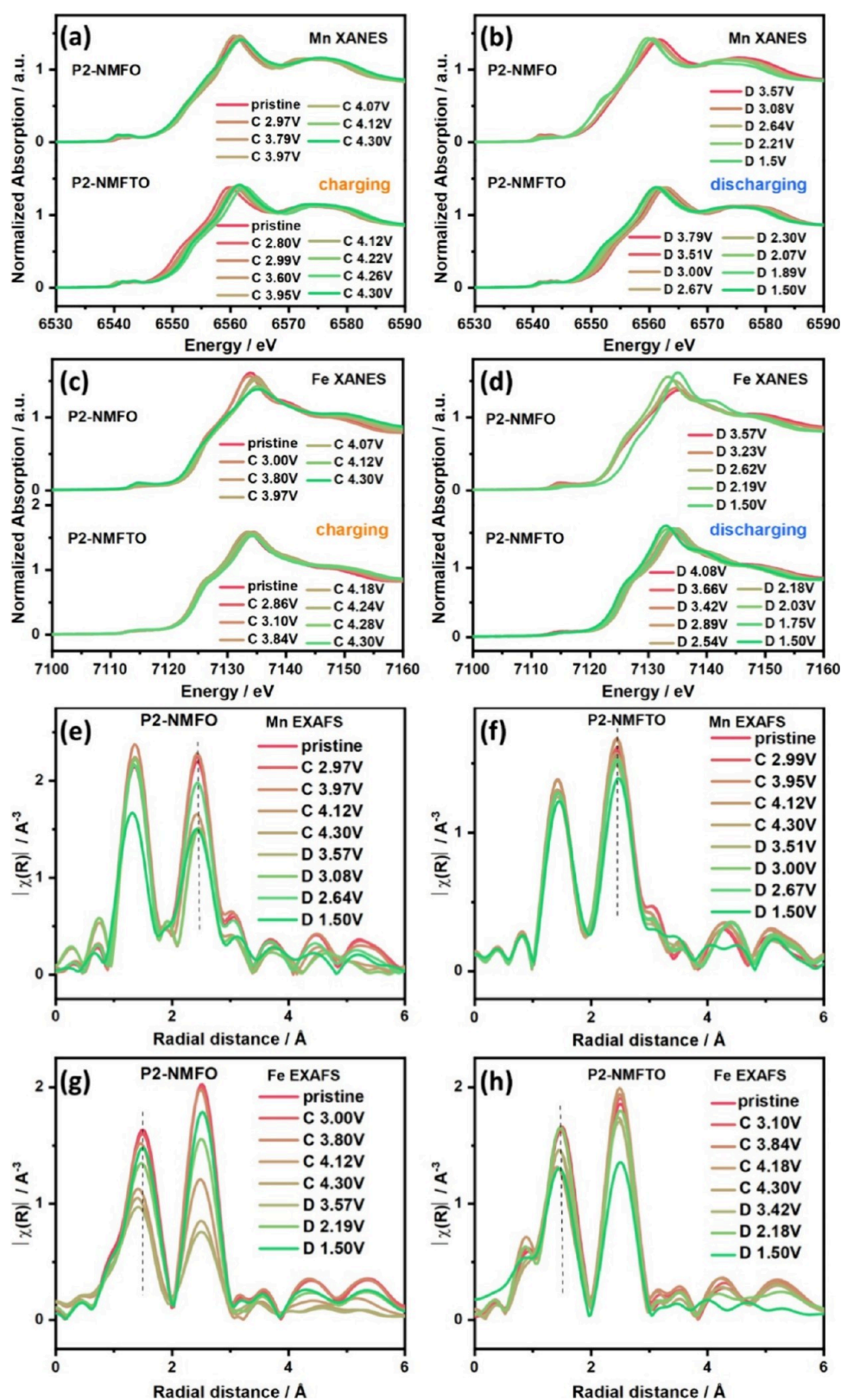
Figure 5. XANES spectra at the Mn K-edge during charging (a) and discharging (b). XANES spectra at the Fe K-edge during charging (c) and discharging (d). (e) Fourier transforms (k^3-weighted) of the Mn K-edge EXAFS spectra of NMFO. (f) Fourier transforms (k^3-weighted) of the Mn K-edge EXAFS spectra of NMFTO. (g) Fourier transforms (k^3-weighted) of the Fe K-edge EXAFS spectra of NMFO. (h) Fourier transforms (k^3-weighted) of the Fe K-edge EXAFS spectra of NMFTO.

residual intensity is observed for the broad main resonance, in contrast to NMFO. This residual intensity reveals that NMFTO is not completely desodiated by charging to 4.3 V.

The residual Na content observed at 4.3 V explains why the capacity of NMFTO can be further increased by cycling in the larger voltage window of 1.5−4.5 V. During the discharging
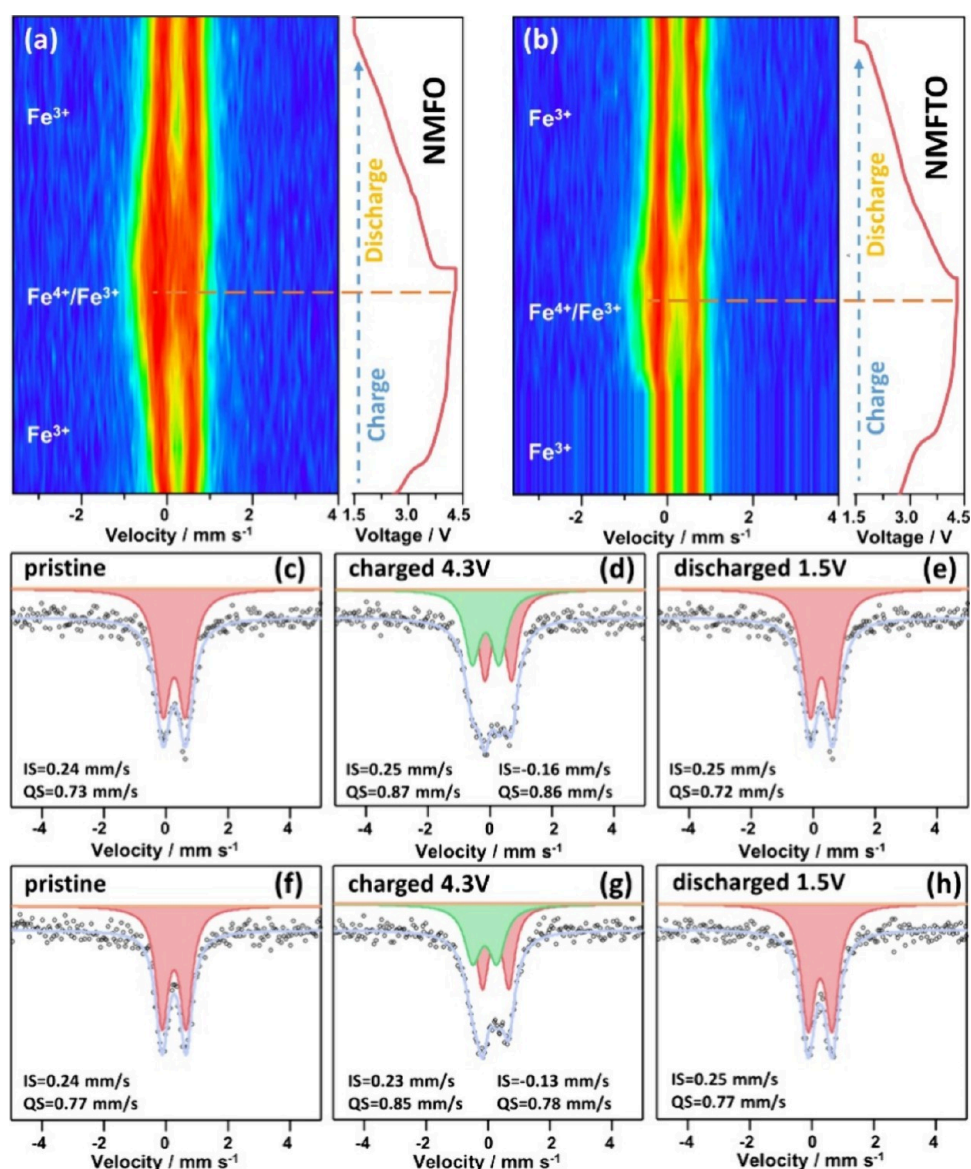
Figure 6. Voltage profiles and contour plots of *in situ* ^{57}Fe Mössbauer spectroscopy on (a) NMFO and (b) NMFTO during cycling between 1.5 and 4.3 V at a rate of 0.05 C. ^{57}Fe Mössbauer spectra of NMFO in different states: (c) pristine, (d) charged to 4.3 V, and (e) discharged to 1.5 V. ^{57}Fe Mössbauer spectra of NMFTO: (f) pristine, (g) charged to 4.3 V, and (h) discharged to 1.5 V. The experimental spectra are shown as black spheres and the fitting as purple lines. Fe^{3+} and Fe^{4+} contributions are shown as red and green doublets, respectively.

period, the resonance shifts back to higher values due to the reduction of Fe and Mn. When the cathode is completely discharged to 2.0 V, the signal becomes very broad and again is difficult to be detected. Also for this material, the overall evolution of the spectra shows that after one complete cycle the material is reduced to a state beyond the initial state, i.e., sodiated to a Na content higher than in the pristine material. This means that the Na content after the first complete cycle is larger than 0.67, maybe close to 1. This is consistent with the length of the first charge/discharge plateaus (the latter one being much longer) and the fact that the voltage after one complete cycle (1.5 V) is smaller than the open-circuit voltage before this cycle (about 2.8 V).

The changes in the electronic structure and local environments of manganese and iron in NMFO and NMFTO during the first cycle are studied by *in situ* XAS. As described above, the average valence of Mn is +3.66 in pristine NMFO and +3.43 in NMFTO. For both materials, the Mn K-edge shifts to

higher energies upon charging (Figure 5a) and shifts back to lower energies throughout the whole discharging process (Figure 5b), indicating the continuous oxidation and reduction of Mn during charging/discharging. Figure S12e shows the linear combination fitting for the variations of Mn^{3+}/Mn^{4+} contents during cycling, which corresponds to the XANES data described above. As seen from this figure, Mn is almost completely oxidized to Mn^{4+} at the end of the charge and reduced to Mn^{3+}/Mn^{4+} with a ratio of about 1:1 at the end of discharge. However, for NMFTO, Mn is not fully oxidized to Mn^{4+} at the end of charging and is reduced to Mn^{3+}/Mn^{4+} with a ratio of about 0.7:0.3 at the end of discharging. Nevertheless, due to the larger Mn content of NMFTO, this contributes to the larger discharge capacity. The Fe K-edge for both materials also shifts to higher energies upon charging (Figure 5c) and shifts back to lower energies upon discharging (Figure 5d), again revealing the reversible oxidation and reduction of Fe.
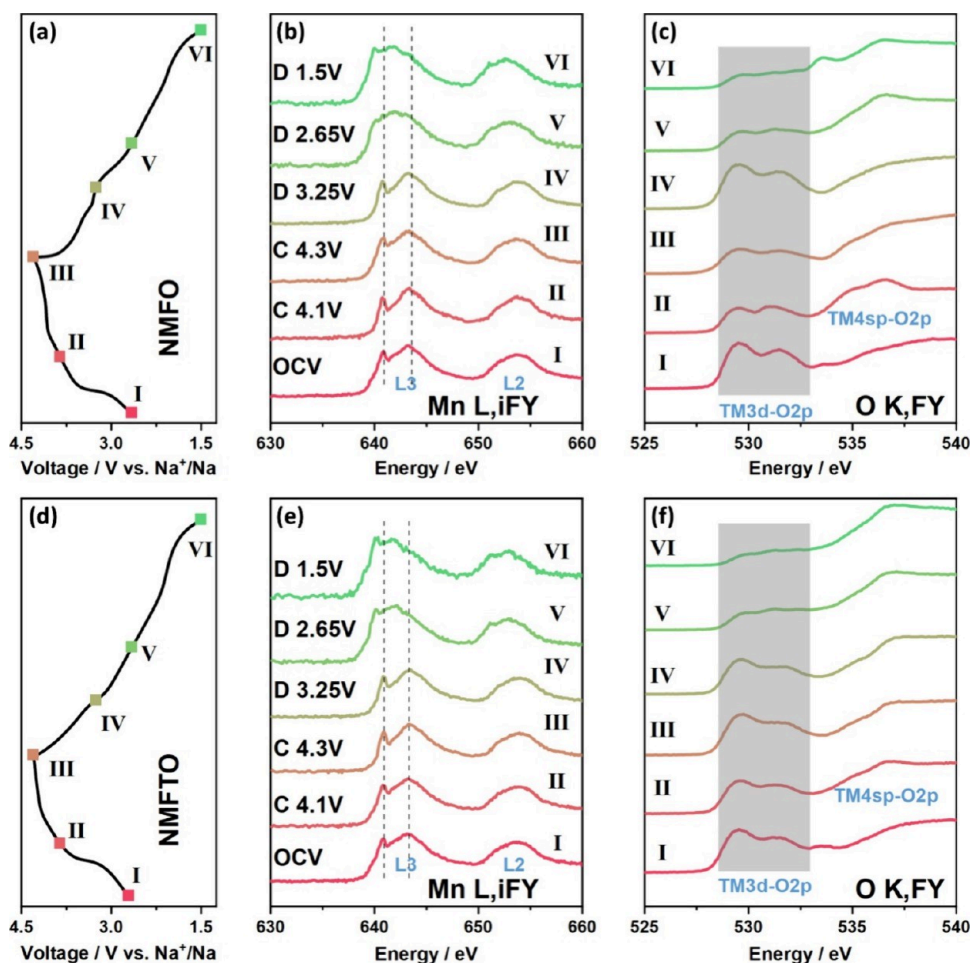
Figure 7. Cell voltage as a function of state of charge and discharge for the first galvanostatic cycle of (a) NMFO and (d) NMFTO cells; marked points indicate voltages at which cells were disassembled for soft XAS measurements. Mn $L_{2,3}$ (b) and O K (c) NEXAFS spectra of NMFO at different voltages. Mn $L_{2,3}$ (e) and O K (f) NEXAFS spectra of NMFTO at different voltages.

Selected *in situ* XANES spectra in the pristine, fully charged, and fully discharged state confirm this tendency (Figure S12b).

The Mn K-edge and Fe K-edge Fourier-transformed (k^3-weighted) EXAFS (FT-EXAFS) spectra acquired during charging/discharging are shown in Figure 5 (e,f: Mn K-edge; g,h: Fe K-edge). There are two peaks at about 1.3 and 2.3 Å in the radial distributions, corresponding to the TM-O distance and the TM-TM/Na distance, respectively. For NMFO, the amplitude of the Mn−O peak (at 1.3 Å) is higher than that of the Mn-TM peak, while the opposite behavior is observed for NMFTO. The change of this Mn−O peak during discharging is very weak for NMFTO, while for NMFO, a strong decrease in intensity occurs in the voltage range from 2.21 to 1.5 V. This strong change can be ascribed to the changes in the local Jahn−Teller distortions around Mn^{3+} during charging/discharging and also the phase change observed via XRD in the highly discharged states. The shift of the second Mn-TM peak (at 2.5 Å) to a larger value, observed for NMFO and NMFTO, indicates the increase of the Mn-TM distance. This is consistent with the changes in the *a* lattice constant observed by SRD, as described above. For NMFTO, the Mn−O and Mn-TM bond length variations are fully reversible, as observed in the subsequent discharging process, and the interatomic distances return to their initial values. For NMFO, a clear decrease in the intensity of the Mn−O peak (at 1.3 Å) at the very end of discharging (Figure 5e and Figure S12c) is

observed. This strong decrease in intensity is not observed for NMFTO. One reason is that the changes in Mn oxidation state during charging/discharging are smaller for NMFTO (pristine: +3.43, fully charged: +3.67, fully discharged: 3.34) compared to NMFO (pristine: +3.66, fully charged: +4, fully discharged: 3.55), as revealed by EXAFS fitting (Table S4).

In summary, our XAS results show that the incorporation of Ti/Mn does not decrease the Jahn−Teller distortion itself but it decreases the changes in the Jahn−Teller distortion during charging/discharging. Furthermore, the presence of inactive Ti^{4+} seems to additionally alleviate the changes in the Jahn−Teller distortion resulting in better cycling stability.

The intensities of the Fe−O peak are lower than those of the Fe-TM peak for both materials. The variations in the Fe−O and Fe-TM bond lengths of both materials are not completely reversible, as shown in Figure S12d. When the spectrum in the pristine state is compared with that in the fully charged state, the radial distribution of NMFO shows a decrease in the Fe−O distance and a reduced intensity of the Fe-TM peak during charging. Meanwhile, the increase in the intensity of the pre-edge peak in the Fe K-edge XANES spectra indicates the migration of a small fraction of Fe ions into interlayer P2-tetrahedral sites at voltages higher than 4.1 V[20].

In situ ^{57}Fe Mössbauer spectroscopy on complete cells during cycling was performed to investigate the change of Fe oxidation state as displayed in Figure 6. Cycling of the cells was
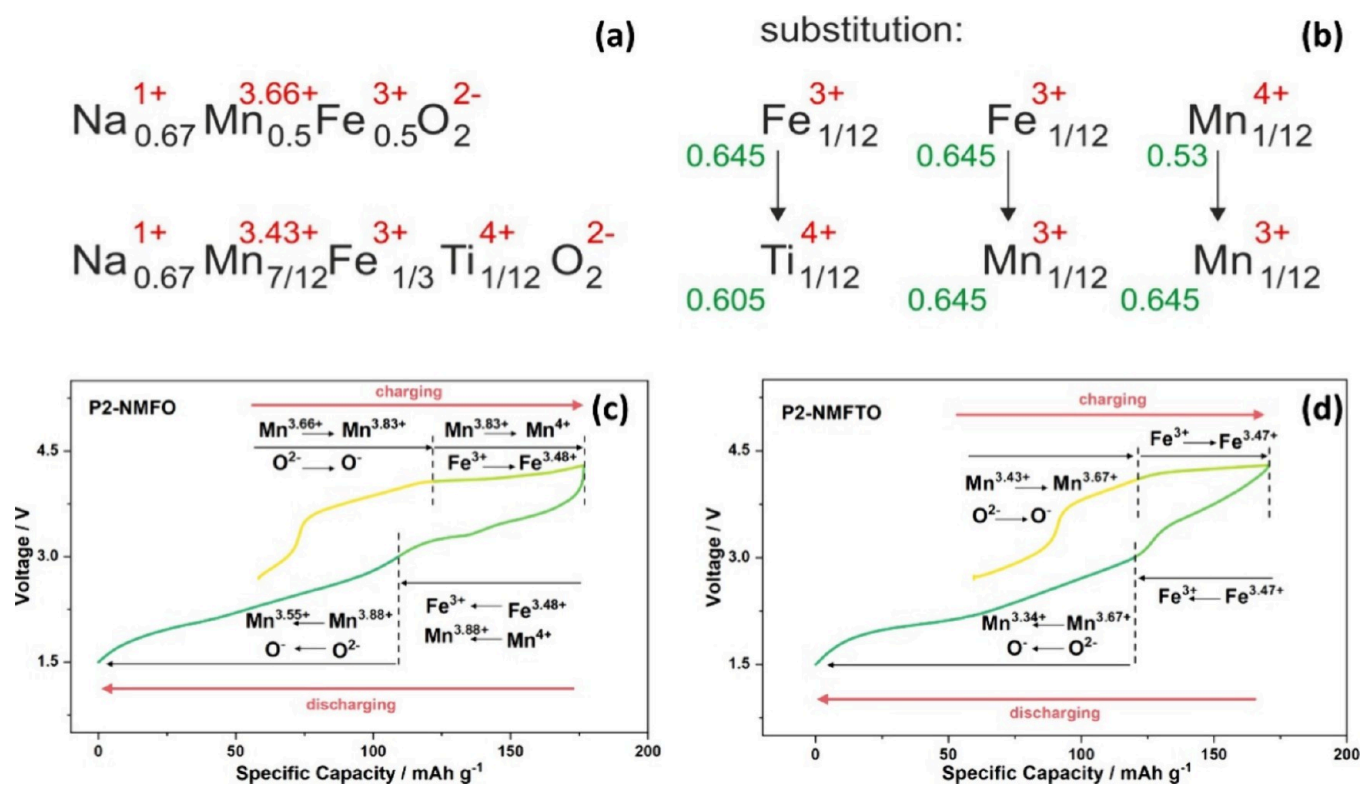
Figure 8. (a) Overall chemical compositions of the two samples NMFO and NMFTO as determined from elemental analysis, (b) corresponding consequences for the changes in the Fe/Mn oxidation states caused by the cosubstitution; green numbers give the ionic radii, (c) summary of the redox processes occurring during charging/discharging in NMFO as observed by the multiple characterization techniques, and (d) the redox processes occurring in NMFTO.

evaluated in the voltage range of 1.5−4.3 V, and one Mössbauer spectrum was acquired every 2 h. The voltage profiles and contour plots of *in situ* ^{57}Fe Mössbauer spectroscopy during the first cycle are shown in Figure 6a (NMFO) and Figure 6b (NMFTO). For both cathodes, the contour plots clearly show the reversible partial conversion of Fe^{3+} to Fe^{4+} and back to Fe^{3+} during the cycling. The detailed parameters resulting from fitting all ^{57}Fe Mössbauer spectra are shown in Figure S13.

As shown in Figure 6c,f, the spectra for both pristine materials exhibit a single sharp doublet with an isomer shift (IS) around ∼0.24 mm s^{-1} consistent with Fe^{3+} in a high-spin state and in an octahedral environment of oxygen. The quadrupolar splitting (QS) of NMFTO is around 0.77 mm s^{-1} and is larger than that of unsubstituted NMFO (0.73 mm s^{-1}), revealing a less symmetric environment. As can be seen from the contour plots, during charging a new component appears in the spectra with negative isomer shift that can be assigned to Fe^{4+}.[46] A higher amount of Fe^{4+} is observed for NMFO at the end of charging in comparison to NMFTO (Figure S13). This might be related to the larger overall Fe content in NMFO where a larger fraction of the specific capacity is based on the Fe^{3+}/Fe^{4+} redox activity. The oxidation/reduction kinetics of Fe^{3+}/Fe^{4+} can be very sluggish.[46] Therefore, for NMFTO, where a larger fraction of the charge−discharge capacity is based on Mn^{3+}/Mn^{4+}, the cycling is more stable. The spectra of NMFO and NMFTO in the fully discharged state (Figure 6e,h) are very similar to those of the pristine materials with almost identical IS and QS values, demonstrating the complete reduction back to Fe^{3+} and thus the high reversibility of this redox process. The spectra of the charged materials (Figure

6d,g) were fitted by using two doublets. The first component is ascribed to $Fe^{3+}O_6$ in an octahedral environment with isomer shift IS very similar to that of the pristine material while the quadrupole splitting QS is larger compared to the pristine materials, revealing local distortions of the octahedral environment around Fe. The second doublet with negative isomer shift clearly reveals the existence of Fe^{4+}, and all Fe^{4+} is reduced back to Fe^{3+} during discharging. The Fe^{4+} doublet observed in the charged state of NMFO shows a larger isomer shift and a larger quadrupole splitting than that of NMFTO, revealing stronger local distortions.

Ex situ soft XAS measurements were performed on NMFO and NMFTO cathodes extracted from cells at different voltages during the first cycle (Figure 7a,d) to predict changes in the oxidation states and chemical environments. The Mn L-edge XAS spectra acquired in the inverse fluorescence yield (iFY) mode are shown in Figure 7b,e. Enlarged views of Mn $L_{2,3}$ NEXAFS spectra of NMFO and NMFTO at different voltages are shown in Figure S14a,b. The peak at 642 eV is ascribed to Mn^{3+} and the peaks at 641 and 643 eV correspond to Mn^{4+}.[47] The spectra for both cathodes obtained in the pristine state demonstrate that Mn exists in a mixed oxidation state, Mn^{3+}/Mn^{4+}, which is in good agreement with the results on the Mn K-edge described above. The spectra show no pronounced change in the fully charged state. However, during discharging, when the potential reaches 2.65 V, the spectra of both materials predominantly show the Mn^{3+} peak. The L_3-edge (observed at 643 eV) of both materials shows almost no change when going from 2.65 to 1.5 V. However, for the L_2-edge (observed at 653.6 eV), the spectra of NMFTO have clearer features of Mn^{3+}, which indicates that Mn in NMFTO

can be reduced to lower valence states, in agreement with the result obtained by linear combination fitting of *in situ* XAS Mn K-edge data (Figure S12e). The Fe L-edge XAS spectra in the iFY mode for these samples are shown in Figure S15a,b. The Fe L-edge spectra of both pristine materials show obvious features of Fe^{3+},[48] in good agreement with the Mössbauer results. However, no big changes can be observed during charging. We ascribe this to the fact that these measurements are performed *ex situ* and the stability of Fe^{4+} seems to be limited outside the batteries.[49] The changes in the Fe oxidation state during cycling can thus be much better observed by the *in situ* Mössbauer measurements.

The O K-edge XAS spectra acquired in the fluorescence yield (FY) mode are shown in Figure 7c,f. Enlarged views of O K-edge XAS spectra of NMFO and NMFTO at different voltages are shown in Figure S16a,b. For the O K-edge, the pre-edge peaks below 535 eV are related to the hybridization of O 2p-TM 3d orbitals, while the broad peak above 535 eV is related to O 2p-TM 4sp hybridized states. The peaks around 529.4 and 531.3 eV correspond to contributions from the t_{2g} band and the e_g band, respectively. Because the density of the empty bound state in the molecular energy level is related to the hybridization of metal 3d-O 2p orbitals, the variation of integrated pre-edge intensity (shadow region in Figure 7c,f) can show the hole state distribution and the effective charge on the oxygen atom.[50] The integrated intensity that reflects the changes in the density of empty states was calculated and is displayed in Figure S17. For NMFO, the intensity of the integrated pre-edge (Figure S17a) shows irregular changes during the charging and discharging process, which are caused by gliding of TMO_2 slabs during the phase change process, as observed in the in situ XRD measurements described above. However, for NMFTO, the intensity of integrated pre-edge (Figure S17b) shows more regular changes during the electrochemical cycling, which is relevant to electron removal from oxygen and the consequently generated holes in O 2p orbitals.[51] So the anionic contribtion to the charge/discharge capacity can be observed from this integrated pre-edge intensity for NMFTO, while it is somehow obscured by the stronger crystallographic changes for NMFO.

Galvanostatic intermittent titration technique (GITT) is used to estimate the diffusion coefficient of Na^+ and thus to verify the fact that Ti substitution enhances the transport channels. Figure S18a,b shows the details of the GITT measurement during the charging and discharging of NMFO. GITT tests are performed with a 0.5 h current pulse at C/20 followed by 5 h relaxation for every step and the results are shown in Figure S18c (NMFO) and Figure S18d (NMFTO). The overall charge/discharge capacities obtained during this GITT measurements show no big differences between the two samples. However, the voltage plateau of NMFTO is suppressed, which can be explained by Mn/Ti-substitution delaying the phase transition. The normalized quantity $D_s S^2 / V_m^2$ was used to represent the change in Na mobility because it is challenging to get the exact values for the molar volume and the active surface area, as shown in Figure S18e (charging) and Figure S18f (discharging). Compared with NMFO, the substituted NMFTO shows higher $D_s S^2 / V_m^2$ values both during charging and discharging, which indicates a higher Na^+ mobility induced by Mn/Ti substitution.[42]

The results of the multiple characterization techniques are summarized in Figure 8. For the cosubstitution described in this manuscript, when going from NMFO to NMFTO, 1/12 of Fe per formula unit is replaced by Ti and 1/12 of Fe per formula unit is replaced by Mn. The Mössbauer results (Figure 6) clearly show that the pristine NMFO and NMFTO samples contain exclusively trivalent Fe ions. The soft-XAS measurements reveal that Ti is present exclusively as tetravalent ions. From this, assuming the oxidation states of Na and O to be 1+ and 2−, respectively, the average oxidation state of Mn can be determined to be 3.66+ for NMFO and 3.43+ for NMFTO.

Furthermore, Figure 8c,d shows the summary of all conclusions from the different experimental techniques. For NMFTO, the XAS results clearly show that Mn is active in the beginning of charging and at the end of discharging (Figure S12). The Mössbauer results clearly show that for NMFTO Fe is active at the end of charging and at the beginning of discharging. For NMFO similar trends are observed, although the changes in the Mn oxidation state in the beginning of charging are less obvious, probably due to the higher initial Mn oxidation state compared to NMFTO, resulting in a smaller Mn contribution to the charge capacity, as also revealed by the shorter plateau observed around 3.0 V.

A single-electron redox process of a Mn^{3+}/Mn^{4+} couple in NMFO (0.5 Mn per formular unit) corresponds to a specific capacity of around 133.5 mAh g^{-1}. Taking together the linear combination fitting of the *in situ* Mn K-edge XAS measurements with the results of Fe Mössbauer spectroscopy, during charging from the OCV to 4.07 V, the theoretical capacity based on oxidation of $Mn^{3.66+}$ to $Mn^{3.83+}$ corresponds to around 23 mAh g^{-1}. The remaining 41 mAh g^{-1} observed during charging from the OCV to 4.07 V can be attributed to the oxidation of oxygen ions. It is known for overlithiated Li cathodes, that the contributions from oxygen during charging/discharging can cover a large range of voltages, including annihilation of eletron holes in the oxygen 2p band (around 4.3 V^{52-55}) and reversible $O^{2-/n-}$ contributions (around 3.3 $V^{52,54,56,57}$). The theoretical capacity based on a single-electron redox process of an Fe^{3+}/Fe^{4+} couple in NMFO (0.5 Fe per formula unit) is 133.5 mAh g^{-1}. From 4.07 to 4.3 V, the area ratio of Fe^{4+}:Fe^{3+} is 0.48:0.52, which means that the contribution of Fe^{3+} oxidation is around 64 mAh g^{-1}, which is somewhat larger than the observed capacity of 46 mAh g^{-1}. The reason might be that the different cationic/anionic contributions are overlapping, possibly due to sluggish kinetics, and cannot be clearly separated. Furthermore, at these high voltages, mixed metal/oxygen hybride orbitals might be involved. Therefore, the exact contributions from the cations and anions, as indicated in Figure 8c,d, should be taken with care. From 4.07 to 4.3 V, the oxidation of a $Mn^{3.83+}/Mn^{4+}$ couple should also provide 23 mAh g^{-1}. During the discharging period, from 4.3 to 3.0 V, the capacity of $Fe^{3.48+}$ reduction is 64 mAh g^{-1} and the capacity of reduction from Mn^{4+} to $Mn^{3.88+}$ is 16 mAh g^{-1}. From 3.0 to 1.5 V, the theoretical capacity based on reduction of $Mn^{3.88+}$ to $Mn^{3.55+}$ is around 44 mAh g^{-1}. The additionally observed capacity can be attributed to contributions from oxygen ions.

A single-electron redox process of a Mn^{3+}/Mn^{4+} couple in NMFTO (0.58 Mn per formula unit) corresponds to 155 mAh g^{-1}. Combining the linear combination fitting of the *in situ* Mn K-edge XAS measurements with the results of Fe Mössbauer spectroscopy, during charging from OCV to 4.1 V, the theoretical capacity based on oxidation of $Mn^{3.43+}$ to $Mn^{3.67+}$ is around 37 mAh g^{-1}. The remaining 25 mAh g^{-1} observed from the OCV to 4.1 V can be attributed to the oxidation of oxygen ions. The theoretical capacity based on a single-electron redox

process of a Fe^{3+}/Fe^{4+} couple in NMFTO (0.33 Fe per formula unit) is 90 mAh g^{-1}. From 4.1 to 4.3 V, the area ratio of Fe^{4+}: Fe^{3+} is 0.47:0.53, which means that the theoretical capacity of Fe^{3+} oxidation is around 42 mAh g^{-1}, which is in good agreement with the observed capacity of 48 mAh g^{-1}. During discharging from 4.3 to 3.0 V, the capacity of $Fe^{3.47+}$ reduction is 50 mAh g^{-1}, which is very close to the capacity of Fe^{3+} oxidation during charging. The reduction of $Mn^{3.67+}$ starts at 3.0 V. From 3.0 to 1.5 V, the theoretical capacity based on reduction of $Mn^{3.67+}$ to $Mn^{3.34+}$ is around 51 mAh g^{-1}. The additionally observed capacity can be attributed to contributions from the oxygen ions.

4. CONCLUSIONS

In summary, we have investigated the redox reactions of transition metals and oxygen to explain the mechanism of the electrochemical performance of P2-type Mn/Fe based layered cathodes. We introduce P2-NMFTO as the cathode to overcome the short cycle life and poor rate capability caused by the phase changes at high potentials and the Jahn–Teller effect at low potentials, which are both related to Mn oxidation/reduction. The partial substitution of Fe by Mn and Ti has been done to explore and optimize the mechanism of redox activity of these P2-type Mn/Fe based layered cathodes without phase changes. The Mn substitution suppresses the phase transition from the P2-type to the Z-type at high voltages. At the same time, Ti substitution in NMFO can suppress the formation of the P′2 phase at low voltages, thus improving the capacity retention during cycling and increasing the structural stability in the wider potential voltage from 1.5 to 4.5 V.

■ ASSOCIATED CONTENT

ⓢ Supporting Information

The Supporting Information is available free of charge at https://pubs.acs.org/doi/10.1021/acs.chemmater.3c01552.

> SEM images with EDX mapping; HAADF-STEM images with elemental mapping; voltage profiles and galvanostatic cycling; dQ/dV plots; selected XRD patterns from *in situ* XRD measurments; ^{23}Na NMR spectra; linear combination fitting of *in situ* XAS data; fit parameters of *in situ* Mössbauer data; enlarged views of soft XAS data; GITT measurments; ICP-OES data; details of Rietveld refinement; comparison of cycling performance with literature data; EXAFS fitting (PDF)

■ AUTHOR INFORMATION

Corresponding Author

Sylvio Indris − *Institute for Applied Materials (IAM), Karlsruhe Institute of Technology (KIT), 76344 Eggenstein-Leopoldshafen, Germany; Applied Chemistry and Engineering Research Centre of Excellence (ACER CoE), Université Mohammed VI Polytechnic (UM6P), Ben Guerir 43150, Morocco;* orcid.org/0000-0002-5100-113X; Phone: +49-721-680-28508; Email: sylvio.indris@kit.edu

Authors

Jiali Peng − *Institute for Applied Materials (IAM), Karlsruhe Institute of Technology (KIT), 76344 Eggenstein-Leopoldshafen, Germany*

Angelina Sarapulova − *Institute for Applied Materials (IAM), Karlsruhe Institute of Technology (KIT), 76344 Eggenstein-*

Leopoldshafen, Germany; orcid.org/0000-0003-4643-3912

Qiang Fu − *Institute for Applied Materials (IAM), Karlsruhe Institute of Technology (KIT), 76344 Eggenstein-Leopoldshafen, Germany*

Hang Li − *Institute for Applied Materials (IAM), Karlsruhe Institute of Technology (KIT), 76344 Eggenstein-Leopoldshafen, Germany*

Hao Liu − *Institute for Applied Materials (IAM), Karlsruhe Institute of Technology (KIT), 76344 Eggenstein-Leopoldshafen, Germany*

Oleksandr Dolotko − *Institute for Applied Materials (IAM), Karlsruhe Institute of Technology (KIT), 76344 Eggenstein-Leopoldshafen, Germany*

Thomas Bergfeldt − *Institute for Applied Materials (IAM), Karlsruhe Institute of Technology (KIT), 76344 Eggenstein-Leopoldshafen, Germany*

Karin Kleiner − *Münster Electrochemical Energy Technology (MEET), University of Münster (WWU), 48149 Münster, Germany*

Bixian Ying − *Münster Electrochemical Energy Technology (MEET), University of Münster (WWU), 48149 Münster, Germany*

Yi Wu − *SEU-FEI Nan-Center, Key Laboratory of MEMS of Ministry of Education, Southeast University, Nanjing 210096, China*

Volodymyr Baran − *Deutsches Elektronen-Synchrotron (DESY), 22607 Hamburg, Germany;* orcid.org/0000-0003-2379-3632

Edmund Welter − *Deutsches Elektronen-Synchrotron (DESY), 22607 Hamburg, Germany*

Peter Nagel − *Institute for Quantum Materials and Technologies (IQMT), Karlsruhe Institute of Technology (KIT), 76021 Karlsruhe, Germany; Karlsruhe Nano Micro Facility (KNMFi), Karlsruhe Institute of Technology (KIT), 76344 Eggenstein-Leopoldshafen, Germany*

Stefan Schuppler − *Institute for Quantum Materials and Technologies (IQMT), Karlsruhe Institute of Technology (KIT), 76021 Karlsruhe, Germany; Karlsruhe Nano Micro Facility (KNMFi), Karlsruhe Institute of Technology (KIT), 76344 Eggenstein-Leopoldshafen, Germany*

Michael Merz − *Institute for Quantum Materials and Technologies (IQMT), Karlsruhe Institute of Technology (KIT), 76021 Karlsruhe, Germany; Karlsruhe Nano Micro Facility (KNMFi), Karlsruhe Institute of Technology (KIT), 76344 Eggenstein-Leopoldshafen, Germany;* orcid.org/0000-0002-7346-7176

Michael Knapp − *Institute for Applied Materials (IAM), Karlsruhe Institute of Technology (KIT), 76344 Eggenstein-Leopoldshafen, Germany;* orcid.org/0000-0003-0091-8463

Helmut Ehrenberg − *Institute for Applied Materials (IAM), Karlsruhe Institute of Technology (KIT), 76344 Eggenstein-Leopoldshafen, Germany;* orcid.org/0000-0002-5134-7130

Complete contact information is available at:
https://pubs.acs.org/10.1021/acs.chemmater.3c01552

Notes

The authors declare no competing financial interest.

■ REFERENCES

(1) Tarascon, J.-M. Na-ion versus Li-ion Batteries: Complementarity Rather than Competitiveness. *Joule* 2020, *4* (8), 1613−1620.

(2) Park, Y. J.; Choi, J. U.; Jo, J. H.; Jo, C.-H.; Kim, J.; Myung, S.-T. A New Strategy to Build a High-Performance P′2-Type Cathode Material through Titanium Doping for Sodium-Ion Batteries. *Adv. Funct. Mater.* 2019, *29* (28), 1901912.

(3) Dunn, B.; Kamath, H.; Tarascon, J. M. Electrical Energy Storage for the Grid: a Battery of Choices. *Science* 2011, *334* (6058), 928−35.

(4) Liu, Q.; Hu, Z.; Chen, M.; Zou, C.; Jin, H.; Wang, S.; Chou, S. L.; Liu, Y.; Dou, S.-X. The Cathode Choice for Commercialization of Sodium-Ion Batteries: Layered Transition Metal Oxides versus Prussian Blue Analogs. *Adv. Funct. Mater.* 2020, *30* (14), 1909530.

(5) Liu, Q.; Hu, Z.; Chen, M.; Zou, C.; Jin, H.; Wang, S.; Chou, S.-L.; Dou, S.-X. Recent Progress of Layered Transition Metal Oxide Cathodes for Sodium-Ion Batteries. *Small* 2019, *15* (32), e1805381.

(6) Delmas, C.; Carlier, D.; Guignard, M. The Layered Oxides in Lithium and Sodium-Ion Batteries: A Solid-State Chemistry Approach. *Adv. Energy Mater.* 2020, *11* (2), 2001201 DOI: 10.1002/aenm.202001201.

(7) Kubota, K.; Kumakura, S.; Yoda, Y.; Kuroki, K.; Komaba, S. Electrochemistry and Solid-State Chemistry of NaMeO₂ (Me = 3d Transition Metals). *Adv. Energy Mater.* 2018, *8* (17), 1703415.

(8) Kundu, D.; Talaie, E.; Duffort, V.; Nazar, L. F. The Emerging Chemistry of Sodium Ion Batteries for Electrochemical Energy Storage. *Angew. Chem., Int. Ed.* 2015, *54* (11), 3431−48.

(9) Delmas, C.; Fouassier, C.; Hagenmuller, P. Structural Classification and Properties of the Layered Oxides. *Physica B+C* 1980, *99* (1−4), 81−85.

(10) Kumakura, S.; Tahara, Y.; Kubota, K.; Chihara, K.; Komaba, S. Sodium and Manganese Stoichiometry of P2-Type Na2/3 MnO2. *Angew. Chem., Int. Ed. Engl.* 2016, *55* (41), 12760−3.

(11) Keller, M.; Buchholz, D.; Passerini, S. Layered Na-Ion Cathodes with Outstanding Performance Resulting from the Synergetic Effect of Mixed P- and O-Type Phases. *Adv. Energy. Mater.* 2016, *6* (3), 1501555.

(12) Yao, H.; Lv, W.; Yuan, X.; Guo, Y.; Zheng, L.; Yang, X.; Li, J.; Huang, Y.; Huang, Z.; Wang, P.; Guo, Y. New Insights to Build Na^+/Vacancy Disordering for High-Performance P2-Type Layered Oxide Cathodes. *Nano Energy* 2022, *97*, No. 107207.

(13) Talaie, E.; Duffort, V.; Smith, L. H.; Fultz, B.; Nazar, F. L. Structure of the High Voltage Phase of Layered P2-$Na_{2/3-z}Mn_{1/2}Fe_{1/2}O_2$ and the positive effect of Ni Substitution on its Stability. *Energy Environ. Sci.* 2015, *8* (8), 2512.

(14) Kim, D.; Kang, S.-H.; Slater, M.; Rood, S.; Vaughey, J. T.; Karan, N.; Balasubramanian, M.; Johnson, C. S. Enabling Sodium Batteries Using Lithium-Substituted Sodium Layered Transition Metal Oxide Cathodes. *Adv. Energy Mater.* 2011, *1* (3), 333−336.

(15) Yabuuchi, N.; Kajiyama, M.; Iwatate, J.; Nishikawa, H.; Hitomi, S.; Okuyama, R.; Usui, R.; Yamada, Y.; Komaba, S. P2-type $Na_{(x)}[Fe_{(1/2)}Mn_{(1/2)}]O_2$ Made from Earth-Abundant Elements for Rechargeable Na Batteries. *Nat. Mater.* 2012, *11* (6), 512−7.

(16) Yang, Q.; Wang, P. F.; Guo, J. Z.; Chen, Z. M.; Pang, W. L.; Huang, K. C.; Guo, Y. G.; Wu, X. L.; Zhang, J. P. Advanced P2-$Na_{2/3}Ni_{1/3}Mn_{7/12}Fe_{1/12}O_2$ Cathode Material with Suppressed P2-O2 Phase Transition toward High-Performance Sodium-Ion Battery. *ACS Appl. Mater. Interfaces* 2018, *10* (40), 34272−34282.

(17) Zhang, G.; Li, J.; Fan, Y.; Liu, Y.; Zhang, P.; Shi, X.; Ma, J.; Zhang, R.; Huang, Y. Suppressed P2-P2′ Phase Transition of Fe/Mn-Based Layered Oxide Cathode for High-Performance Sodium-Ion Batteries. *Energy Storage Mater.* 2022, *51*, 559−567.

(18) Darbar, D.; Reddy, M. V.; Bhattacharya, I. Understanding the Effect of Zn Doping on Stability of Cobalt-Free P2-$Na_{0.60}Fe_{0.5}Mn_{0.5}O_2$ Cathode for Sodium Ion Batteries. *Electrochem.* 2021, *2* (2), 323−334.

(19) Somerville, J. W.; Sobkowiak, A.; Tapia-Ruiz, N.; Billaud, J.; Lozano, J. G.; House, R. A.; Gallington, L. C.; Ericsson, T.; Häggström, L.; Roberts, M. R.; Maitra, U.; Bruce, P. G. Nature of the "Z"-Phase in Layered Na-ion Battery Cathodes. *Energy & Environ. Sci.* 2019, *12* (7), 2223−2232.

(20) Talaie, E.; Kim, S. Y.; Chen, N.; Nazar, L. F. Structural Evolution and Redox Processes Involved in the Electrochemical Cycling of P2-$Na_{0.67}[Mn_{0.66}Fe_{0.20}Cu_{0.14}]O_2$. *Chem. Mater.* 2017, *29* (16), 6684−6697.

(21) Clément, R. J.; Billaud, J.; Armstrong, A. R.; Singh, G.; Rojo, T.; Bruce, P. G.; Grey, C. P. Structurally stable Mg-doped P2-Na2/3Mn1−yMgyO2 sodium-ion battery cathodes with high rate performance: insights from electrochemical, NMR and diffraction studies. *Energy Environ. Sci.* 2016, *9* (10), 3240−3251.

(22) Cheng, Z.; Zhao, B.; Guo, Y.-J.; Yu, L.; Yuan, B.; Hua, W.; Yin, Y.-X.; Xu, S.; Xiao, B.; Han, X.; Wang, P.-F.; Guo, Y.-G. Mitigating the Large-Volume Phase Transition of P2-Type Cathodes by Synergetic Effect of Multiple Ions for Improved Sodium-Ion Batteries. *Adv. Energy Mater.* 2022, *12* (14), 2103461.

(23) Pang, W. K.; Kalluri, S.; Peterson, V. K.; Sharma, N.; Kimpton, J.; Johannessen, B.; Liu, H. K.; Dou, S. X.; Guo, Z. P. Interplay between Electrochemistry and Phase Evolution of the P2-Type $Na_x(Fe_{1/2}Mn_{1/2})O_2$ Cathode for Use in Sodium-Ion Batteries. *Chem. Mater.* 2015, *27* (8), 3150−3158.

(24) Yang, T.; Huang, Y.; Zhang, J.; Zhu, H.; Ren, J.; Li, T.; Gallington, L. C.; Lan, S.; Yang, L.; Liu, Q. Insights into Ti Doping for Stabilizing the $Na_{2/3}Fe_{1/3}Mn_{2/3}O_2$ Cathode in Sodium Ion Battery. *J. Energy Chem.* 2022, *73*, 542−548.

(25) Wang, H.; Gao, R.; Li, Z.; Sun, L.; Hu, Z.; Liu, X. Different Effects of Al Substitution for Mn or Fe on the Structure and Electrochemical Properties of $Na_{0.67}Mn_{0.5}Fe_{0.5}O_2$ as a Sodium Ion Battery Cathode Material. *Inorg. Chem.* 2018, *57* (9), 5249−5257.

(26) Clément, R. J.; Billaud, J.; Robert Armstrong, A.; Singh, G.; Rojo, T.; Bruce, P. G.; Grey, C. P. Structurally Stable Mg-Doped P2-$Na_{2/3}Mn_{1-y}Mg_yO_2$ Sodium-Ion Battery Cathodes with High Rate Performance: Insights from Electrochemical, NMR and Diffraction Studies. *Energy & Environ. Sci.* 2016, *9* (10), 3240−3251.

(27) Ma, C.; Alvarado, J.; Xu, J.; Clement, R. J.; Kodur, M.; Tong, W.; Grey, C. P.; Meng, Y. S. Exploring Oxygen Activity in the High Energy P2-Type $Na_{0.78}Ni_{0.23}Mn_{0.69}O_2$ Cathode Material for Na-Ion Batteries. *J. Am. Chem. Soc.* 2017, *139* (13), 4835−4845.

(28) Maitra, U.; House, R. A.; Somerville, J. W.; Tapia-Ruiz, N.; Lozano, J. G.; Guerrini, N.; Hao, R.; Luo, K.; Jin, L.; Perez-Osorio, M. A.; Massel, F.; Pickup, D. M.; Ramos, S.; Lu, X.; McNally, D. E.; Chadwick, A. V.; Giustino, F.; Schmitt, T.; Duda, L. C.; Roberts, M. R.; Bruce, P. G. Oxygen Redox Chemistry without Excess Alkali-Metal Ions in $Na_{2/3}[Mg_{0.28}Mn_{0.72}]O_2$. *Nat. Chem.* 2018, *10* (3), 288−295.

(29) Mortemard de Boisse, B.; Carlier, D.; Guignard, M.; Bourgeois, L.; Delmas, C. P2-$Na_{(x)}Mn_{(1/2)}Fe_{(1/2)}O_2$ Phase Used as Positive Electrode in Na Batteries: Structural Changes Induced by the Electrochemical (De)intercalation Process. *Inorg. Chem.* 2014, *53* (20), 11197−205.

(30) Rodriguez-Carvajal, J. Recent Advances in Magnetic Structure Determination by Neutron Powder Diffraction. *Phys. B* **1993**, *192*, 55−69.

(31) Bérar, J. F.; Lelann, P. E.s.d.'s and Estimated Probable Error Obtained in Rietveld Refinements with Local Correlations. *J. Appl. Crystallogr.* **1991**, *24* (1), 1−5.

(32) Dippel, A. C.; Liermann, H. P.; Delitz, J. T.; Walter, P.; Schulte-Schrepping, H.; Seeck, O. H.; Franz, H. Beamline P02.1 at PETRA III for High-Resolution and High-Energy Powder Diffraction. *J. Synchrotron. Radiat.* **2015**, *22* (3), 675−87.

(33) Filik, J.; Ashton, A. W.; Chang, P. C. Y.; Chater, P. A.; Day, S. J.; Drakopoulos, M.; Gerring, M. W.; Hart, M. L.; Magdysyuk, O. V.; Michalik, S.; Smith, A.; Tang, C. C.; Terrill, N. J.; Wharmby, M. T.; Wilhelm, H. Processing Two-Dimensional X-ray Diffraction and Small-Angle Scattering Data in DAWN 2. *J. Appl. Crystallogr.* **2017**, *50*, 959−966.

(34) Ravel, B.; Newville, M. ATHENA and ARTEMIS Interactive Graphical Data Analysisusing IFEFFIT. *Phys. Scr.* **2005**, *115*, 1007−1010.

(35) Verma, A.; Smith, K.; Santhanagopalan, S.; Abraham, D.; Yao, K. P.; Mukherjee, P. P. Galvanostatic Intermittent Titration and Performance Based Analysis of $LiNi_{0.5}Co_{0.2}Mn_{0.3}O_2$ Cathode. *J. Electrochem. Soc.* **2017**, *164* (13), A3380−A3392.

(36) Delmas, C.; Braconnier, J.; Fouassier, C.; Hagenmuller, P. Electrochemical Intercalation of Sodium in $NaxCoO_2$ Bronzes. *Solid State Ionics* **1981**, *3−4*, 165−169.

(37) Shannon, R. D. Revised Effective Ionic Radii and Systematic Studies of Interatomic Distances in Halides and Chalcogenides. *Acta Crystallogr., Sect. A* **1976**, *32* (5), 751−767.

(38) Li, X.-L.; Wang, T.; Yuan, Y.; Yue, X.-Y.; Wang, Q.-C.; Wang, J.-Y.; Zhong, J.; Lin, R.-Q.; Yao, Y.; Wu, X.-J.; Yu, X.-Q.; Fu, Z.-W.; Xia, Y.-Y.; Yang, X.-Q.; Liu, T.; Amine, K.; Shadike, Z.; Zhou, Y.-N.; Lu, J. Whole-Voltage-Range Oxygen Redox in P2-Layered Cathode Materials for Sodium-Ion Batteries. *Adv. Mater.* **2021**, *33* (13), e2008194.

(39) Li, Z.; Kong, W.; Yu, Y.; Zhang, J.; Wong, D.; Xu, Z.; Chen, Z.; Schulz, C.; Bartkowiak, M.; Liu, X. Tuning Bulk O_2 and Nonbonding Oxygen State for Reversible Anionic Redox Chemistry in P2-Layered Cathodes. *Angew. Chem., Int. Ed.* **2022**, *61* (16), e202115552.

(40) Wu, X.; Chen, C.; Zhao, C.; Liu, H.; Hu, B.; Li, J.; Li, C.; Hu, B. Achieving Long-Enduring High-Voltage Oxygen Redox in P2-Structured Layered Oxide Cathodes by Eliminating Nonlattice Oxygen Redox. *Small* **2023**, *19*, e2300878.

(41) Liu, X.; Zuo, W.; Zheng, B.; Xiang, Y.; Zhou, K.; Xiao, Z.; Shan, P.; Shi, J.; Li, Q.; Zhong, G.; Fu, R.; Yang, Y. $P2-Na_{0.67}Al_xMn_{1-x}O_2$: Cost-Effective, Stable and High-Rate Sodium Electrodes by Suppressing Phase Transitions and Enhancing Sodium Cation Mobility. *Angew. Chem., Int. Ed.* **2019**, *58* (50), 18086−18095.

(42) Li, H.; Hua, W.; Liu-Théato, X.; Fu, Q.; Desmau, M.; Missyul, A.; Knapp, M.; Ehrenberg, H.; Indris, S. New Insights into Lithium Hopping and Ordering in $LiNiO_2$ Cathodes during Li (De)-intercalation. *Chem. Mater.* **2021**, *33* (24), 9546−9559.

(43) Han, M. H.; Gonzalo, E.; Sharma, N.; López del Amo, J. M.; Armand, M.; Avdeev, M.; Saiz Garitaonandia, J. J.; Rojo, T. High-Performance P2-Phase $Na_{2/3}Mn_{0.8}Fe_{0.1}Ti_{0.1}O_2$ Cathode Material for Ambient-Temperature Sodium-Ion Batteries. *Chem. Mater.* **2016**, *28* (1), 106−116.

(44) Grey, C. P.; Dupre, N. NMR Studies of Cathode Materials for Lithium-Ion Rechargeable Batteries. *Chem. Rev.* **2004**, *104* (10), 4493−512.

(45) Pyykkö, P. Year-2008 Nuclear Quadrupole Moments. *Mol. Phys.* **2008**, *106* (16−18), 1965−1974.

(46) Dräger, C.; Sigel, F.; Witte, R.; Kruk, R.; Pfaffmann, L.; Mangold, S.; Mereacre, V.; Knapp, M.; Ehrenberg, H.; Indris, S. Observation of Electrochemically Active Fe^{3+}/Fe^{4+} in $Li-Co_{0.8}Fe_{0.2}MnO_4$ by In Situ Mössbauer Spectroscopy and X-Ray Absorption Spectroscopy. *Phys. Chem. Chem. Phys.* **2019**, *21* (1), 89−95.

(47) Gilbert, B.; Frazer, B. H.; Belz, A.; Conrad, P. G.; Nealson, K. H.; Haskel, D.; Lang, J. C.; Srajer, G.; De Stasio, G. Multiple Scattering Calculations of Bonding and X-ray Absorption Spectroscopy of Manganese Oxides. *J. Phys. Chem. A* **2003**, *107* (16), 2839−2847.

(48) Kim, D. H.; Lee, H. J.; Kim, G.; Koo, Y. S.; Jung, J. H.; Shin, H. J.; Kim, J.-Y.; Kang, J.-S. Interface electronic structures of BaTiO3@X nanoparticles (X=γ-Fe2O3, Fe3O4, α-Fe2O3, and Fe) investigated by XAS and XMCD. *Phys. Rev. B* **2009**, *79* (3), No. 033402, DOI: 10.1103/PhysRevB.79.033402.

(49) Lee, E.; Brown, D. E.; Alp, E. E.; Ren, Y.; Lu, J.; Woo, J.-J.; Johnson, C. S. New Insights into the Performance Degradation of Fe-Based Layered Oxides in Sodium-Ion Batteries: Instability of Fe^{3+}/Fe^{4+} Redox in $α-NaFeO_2$. *Chem. Mater.* **2015**, *27* (19), 6755−6764.

(50) Yoon, W. S.; Balasubramanian, M.; Chung, K. Y.; Yang, X. Q.; McBreen, J.; Grey, C. P.; Fischer, D. A. Investigation of the Charge Compensation Mechanism on the Electrochemically Li-ion Deintercalated $Li_{1-x}Co_{1/3}Ni_{1/3}Mn_{1/3}O_2$ Electrode System by Combination of Soft and Hard X-ray Absorption Spectroscopy. *J. Am. Chem. Soc.* **2005**, *127* (49), 17479−87.

(51) Wang, Q.; Liao, Y.; Jin, X.; Cheng, C.; Chu, S.; Sheng, C.; Zhang, L.; Hu, B.; Guo, S.; Zhou, H. Dual Honeycomb-Superlattice Enables Double-High Activity and Reversibility of Anion Redox for Sodium-Ion Battery Layered Cathodes. *Angew. Chem., Int. Ed.* **2022**, *61* (33), e202206625.

(52) Sigel, F.; Schwarz, B.; Kleiner, K.; Dräger, C.; Esmezjan, L.; Yavuz, M.; Indris, S.; Ehrenberg, H. Thermally Induced Structural Reordering in Li- and Mn-Rich Layered Oxide Li-Ion Cathode Materials. *Chem. Mater.* **2020**, *32*, 1210−1223.

(53) Luo, K.; Roberts, M. R.; Hao, R.; Guerrini, N.; Pickup, D. M.; Liu, Y.-S.; Edström, K.; Guo, J.; Chadwick, A. V.; Duda, L. C.; Bruce, P. G. Charge-Compensation in 3d-Transition-Metal-Oxide Intercalation Cathodes through the Generation of Localized Electron Holes on Oxygen. *Nat. Chem.* **2016**, *8*, 684−691.

(54) Assat, G.; Foix, D.; Delacourt, C.; Iadecola, A.; Dedryvère, R.; Tarascon, J.-M. Fundamental Interplay between Anionic/Cationic Redox Governing the Kinetics and Thermodynamics of Lithium-Rich Cathodes. *Nat. Commun.* **2017**, *8*, 2219.

(55) Hausbrand, R.; Cherkashinin, G.; Ehrenberg, H.; Gröting, M.; Albe, K.; Hess, C.; Jaegermann, W. Fundamental Degradation Mechanisms of Layered Oxide Li-Ion Battery Cathode Materials: Methodology, Insights and Novel Approaches. *Mater. Sci. Eng., B* **2015**, *192*, 3−25.

(56) Sathiya, M.; Rousse, G.; Ramesha, K.; Laisa, C. P.; Vezin, H.; Sougrati, M. T.; Doublet, M.-L.; Foix, D.; Gonbeau, D.; Walker, W.; Prakash, A. S.; Hassin, M. B.; Dupont, L.; Tarascon, J.-M. Reversible Anionic Redox Chemistry in High-Capacity Layered-Oxide Electrodes. *Nat. Mater.* **2013**, *12*, 827−835.

(57) Oishi, M.; Yamanaka, K.; Watanabe, I.; Shimoda, K.; Matsunaga, T.; Arai, H.; Ukyo, Y.; Uchimoto, Y.; Ogumi, Z.; Ohta, T. Direct Observation of Reversible Oxygen Anion Redox Reaction in Li-Rich Manganese Oxide, Li_2MnO_3, Studied by Soft X-Ray Absorption Spectroscopy. *J. Mater. Chem. A* **2016**, *4*, 9293−9302.